

# Absence of logarithmic divergence of the entanglement entropies at the phase transitions of a 2D classical hard rod model

Christophe Chatelain<sup>1</sup> and Andrej Gendiar<sup>2</sup>

<sup>1</sup> Université de Lorraine, CNRS, LPCT, F-54000 Nancy, France

<sup>2</sup> Institute of Physics, Slovak Academy of Sciences, Dúbravská cesta 9, SK-845 11, Bratislava, Slovakia

the date of receipt and acceptance should be inserted later

**Abstract.** Entanglement entropy is a powerful tool to detect continuous, discontinuous and even topological phase transitions in quantum as well as classical systems. In this work, von Neumann and Renyi entanglement entropies are studied numerically for classical lattice models in a square geometry. A cut is made from the center of the square to the midpoint of one of its edges, say the right edge. The entanglement entropies measure the entanglement between the left and right halves of the system. As in the strip geometry, von Neumann and Renyi entanglement entropies diverge logarithmically at the transition point while they display a jump for first-order phase transitions. The analysis is extended to a classical model of non-overlapping finite hard rods deposited on a square lattice for which Monte Carlo simulations have shown that, when the hard rods span over 7 or more lattice sites, a nematic phase appears in the phase diagram between two disordered phases. A new Corner Transfer Matrix Renormalization Group algorithm (CTMRG) is introduced to study this model. No logarithmic divergence of entanglement entropies is observed at the phase transitions in the CTMRG calculation discussed here. We therefore infer that the transitions neither can belong to the Ising universality class, as previously assumed in the literature, nor be discontinuous.

**PACS.** 05.70.Jk Critical point phenomena – 05.10.-a Computational methods in statistical physics and nonlinear dynamics

## 1 Introduction

The quantum entanglement between the two subsystems  $A$  and  $B$  of a macroscopic system has attracted a considerable interest in the last decade [1, 2, 3]. Besides its purely theoretical interest, the entropy that quantifies this entanglement have found some applications, in particular in the identification of phase boundaries as will be discussed in this work. Denoting

$$\rho_A = \text{Tr}_B |\psi_0\rangle\langle\psi_0| \quad (1)$$

the reduced density matrix of subsystem  $A$  in the ground state  $|\psi_0\rangle$  of the system, the von Neumann entanglement entropy of the degrees of freedom of  $A$  with those of subsystem  $B$  is defined as

$$S_A = -\text{Tr} \rho_A \log \rho_A \quad (2)$$

while the Renyi entropies are

$$S_n = \frac{1}{1-n} \log \text{Tr} \rho_A^n. \quad (3)$$

In dimension  $1+1$  and with Open Boundary Conditions, Conformal Field Theory predicts that von Neumann en-

tanglement entropy diverges logarithmically when approaching a critical point [4]

$$S_A = \frac{c}{6} \ln \frac{\xi}{a} + c' \quad (4)$$

where the correlation length  $\xi$  scales with the control parameter  $\delta$  as  $\xi \sim |\delta|^{-\nu}$ . The prefactor is proportional to the central charge  $c$  which is a universal quantity. At the critical point, the entanglement entropy diverges as  $S_A \sim \frac{c}{6} \ln \ell$  with the length  $\ell$  of the subsystem  $A$ . Similarly, Renyi entropies behave as  $S_n \sim \frac{c}{12} \left(1 + \frac{1}{n}\right) \ln \ell$ . As observed numerically for the quantum  $q$ -state Potts chain with  $q > 4$  [5], the entanglement entropy  $S_A$  displays a jump at a first-order phase transition.

Entanglement entropies  $S_A$  are easily obtained in DMRG calculations of quantum spin chains because the reduced density matrix  $\rho_A$  is computed and diagonalized at each iteration. The approach has been extended to two-dimensional classical systems by using the eigenvector  $|\psi_M\rangle$  associated to the largest eigenvalue of the transfer matrix to construct the density matrix as  $\rho = |\psi_M\rangle\langle\psi_M|$  and then the reduced density matrix  $\rho_A$  by a partial trace. When the classical transfer matrix can be interpreted as the evolu-

tion operator in imaginary time of a 1D quantum Hamiltonian [6,7,8,9,10], the entropy  $S_A = -\text{Tr}_A \rho_A \ln \rho_A$  measures the quantum entanglement between the degrees of freedom lying in  $A$  with those in  $B$ . By abuse of language, one may say that  $S_A$  measures the entanglement between the left and right part of the strip on which the classical system lives. The entanglement entropy has proved to be a useful quantity in classical systems: the phase diagram can be determined from the entanglement entropy, even when it involves topological phase transitions [11]. In the CTMRG algorithm, the reduced density matrix of a cut of width  $L/2$  in a square lattice of size  $L \times L$  is constructed as  $\rho_A = C^4 / \text{Tr} C^4$  [12,13]. Moreover, the CTMRG algorithm requires the corner transfer matrix  $C$  to be diagonalized at each iteration. Therefore, the entanglement entropy is computed in practice as  $-\sum_i \lambda_i^4 \ln \lambda_i^4$  where the  $\lambda_i$ 's are proportional to the eigenvalues of  $C$  with the constraint  $\sum_i \lambda_i^4 = 1$ . In the thermodynamic limit, the cut is the same as the one performed in the transfer matrix approach so  $S_A$  measures the entanglement between the left and right halves of the systems or, more precisely, between the left and right halves of the equivalent quantum spin chain.

In this work, the behavior of entanglement entropies are studied for a model of non-overlapping  $k$ -mers deposited on a lattice. The case  $k = 2$  corresponds to the celebrated dimer model that has attracted a lot of interest in the last half-century. Besides its experimental relevance to systems where diatomic molecules are adsorbed on a surface [14], the full covering of a graph by dimers was mostly studied by physicists and mathematicians from a purely theoretical perspective [15,16]. Fisher [17] and Kasteleyn [18] independently managed to express the partition function as a pfaffian and then compute exactly the free energy density of the model. The more general case of a mixture of monomers and dimers was subsequently studied and, thanks to a mapping onto an Ising model, it was shown that the free energy density is an analytic function of the chemical potential of the dimers [19,20]. Therefore, the model does not undergo any phase transition. The same conclusion was drawn for a lattice model of trimers [21]. As recently shown, a Kosterlitz-Thouless phase can nevertheless be observed in the dimer model at close-packing when an interaction is introduced between aligned dimers on the same plaquette of the square lattice [22,23].

On the other hand, a gas of infinitely long rigid polymers is expected to undergo an entropy-driven first-order transition between an isotropic and a nematic phase [24, 25]. A discretization of the orientation of the polymers does not change this conclusion [26]. In 2D, a generalization of the Mermin-Wagner theorem forbids the existence of a nematic phase that would break the symmetry under rotation [27,28]. Monte Carlo simulations of infinitely thin needles have however shown the existence of a Berezinskii-Kosterlitz-Thouless transition [29]. For discrete orientations of the needles, the Mermin-Wagner theorem does

not hold anymore and a nematic phase may be observed.

One may therefore assume that rigid finite polymers, consisting in  $k$  monomers aligned on the lattice, should display an isotropic-nematic phase transition for sufficiently large enough  $k$ . In 2007, Ghosh *et al.* argued that such a model should actually undergo two phase transitions as the chemical potential is increased [31]. Like infinitely long rigid polymers,  $k$ -mers are first expected to undergo a transition between an isotropic and a nematic phase. When approaching close-packing at high chemical potential, the system is expected to return to an isotropic phase. Using Monte Carlo simulations, Ghosh *et al.* showed that this scenario is indeed observed for  $k \geq 7$ . However, such Monte Carlo simulations based on local removal/deposition of a single  $k$ -mer are very difficult due to a large autocorrelation time. Nevertheless, the first isotropic-nematic transition was shown to be continuous with critical exponents compatible with the Ising universality class on the square lattice and the three-state Potts model one on the triangular lattice [32,33,34,35]. This critical behavior is explained by the fact that, in the nematic phase, the  $\mathbb{Z}_q$  symmetry of the different orientations of the  $k$ -mers is spontaneously broken [36]. There are  $q = 2$  possible orientations on the square lattice and  $q = 3$  on the triangular lattice. Later a cluster algorithm updating  $k$ -mers along a whole row or column of the lattice was introduced [37] and allowed for studying the model at high densities. The second nematic-isotropic transition was shown to be continuous too but the estimated critical exponents are incompatible with the Ising universality class. The possibility of a cross-over to Ising universality class at large length scales is however not excluded by the authors.

In this study, the  $k$ -mer model is considered on the square lattice. A new Corner Transfer Matrix Renormalization Group (CTMRG) is introduced to cope with the fact that the Corner Transfer Matrix of the  $k$ -mer model is not symmetric for  $k > 2$ , in contrast to usual lattice spin models. The details of the algorithm are presented in the first section along with the Boundary Conditions chosen to break the symmetry and the different observables estimated to characterize the phase transitions. In particular, the entanglement entropies are introduced. Results for the Ising, Potts and clock models, undergoing respectively continuous, discontinuous and two Berezinskii-Kosterlitz-Thouless transitions, are discussed to allow further comparisons with the 7-mer model. In the second section, numerical data for the 6, 7 and 8-mer models are presented and discussed. In agreement with previous Monte Carlo simulations, the order parameter and the entropy reveals the existence of a nematic phase for  $k \geq 7$ . In the third section, numerical evidence is given that the entanglement entropies of  $k$ -mer model does not diverge at the transitions. Conclusions follow.

## 2 Numerical methodology

In 1968, Baxter introduced the first Matrix-Product-State algorithm for the monomer-dimer model on the square lattice [38]. As in DMRG to be introduced 25 years later [39, 40, 41, 42], the ground state of the classical transfer matrix is approximated by a Matrix-Product-State (MPS). The optimization of this MPS is performed by alternating between the transfer matrices generating the lattice horizontally and vertically respectively. The convergence to a machine-precision accuracy is extremely fast, mainly due to the fact that the model is not critical. Two of the tensors forming the MPS turn out to be corner transfer matrices. Shortly after the introduction of DMRG, an algorithm, based on this corner transfer matrix and known as Corner Transfer Matrix Renormalization-Group algorithm (CTMRG), was introduced for classical systems [43]. Neither the Baxter algorithm nor CTMRG can be applied to  $k$ -mers with  $k > 2$  because the corner transfer matrix is not symmetric in this case. In this paper, a new CTMRG is introduced for the  $k$ -mer model. The symmetry of the corner-transfer matrix is not required anymore. The algorithm exploits the mirror symmetry under reflection with respect to the horizontal or vertical axis to greatly improve the convergence.

### 2.1 Corner Transfer Matrix Renormalization Group algorithm

Each vertex of the square lattice is given a statistical weight  $w(s_1, s_2, s_3, s_4)$  which depends on the states  $s_1, s_2, s_3$  and  $s_4$  of the four incoming bonds. The elements of the transfer matrix  $T$  are defined as the statistical weight of a single row (or column) of vertices. They can be written as a product of  $w$ 's. Using the notations of figure 1, these elements reads

$$\begin{aligned} T^{s_5}(s_1, s_2, \dots; s'_1, s'_2, \dots) \\ = \prod_{s_6, s_7, \dots} w(s_1, s_7, s'_1, s_6) w(s_2, s_8, s'_2, s_7) \dots \end{aligned} \quad (5)$$

Note that the transfer matrix still depends on the state  $s_5$  of the pending bond at the top. Depending on the specific type of boundary conditions we intend to impose, the appropriate setting of the state  $s_6$  needs to be taken. The elements of the corner transfer matrix  $C(s_1, s_2, \dots; s'_1, s'_2, \dots)$  are the statistical weights of a square (see figure 1) [44]. Boundary Conditions have been applied to the bonds on the two opposite sides of the square.

The partition function can be decomposed into one vertex, four transfer matrices  $T_i$  and four corner transfer matrices  $C_i$  as (figure 2)

$$\mathcal{Z} = \sum_{s_1, s_2, s_3, s_4} w(s_1, s_2, s_3, s_4) \text{Tr} [T_1^{s_1} C_1 T_2^{s_2} C_2 T_3^{s_3} C_3 T_4^{s_4} C_4] \quad (6)$$

The four parameters  $s_1, s_2, s_3,$  and  $s_4$  of the vertex correspond to the states of the bonds at the right, top, left and

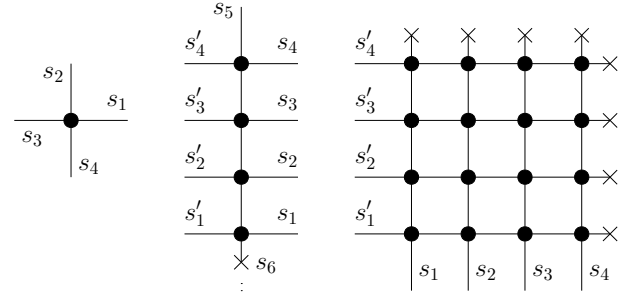


**Fig. 1.** Diagrammatic representation of the vertex  $w$  (left), the transfer matrix  $T$  (center) and the corner transfer matrix  $C$  (right). Each black circle denotes a weight  $w(s_1, s_2, s_3, s_4)$ . The crosses means that some specific boundary conditions are applied: the state of the bond can be fixed or a sum can be performed over all possible values. The sum over the states of all the internal bonds is implicit.

bottom of the vertex. This decomposition is diagrammatically represented on figure 2. The thin lines on the figure correspond to bonds that carry a single degree of freedom. The thick lines carry renormalized states. In the following, we are interested in systems for which the statistical weight of a vertex is symmetric up to a local operation under a mirror transformation with respect to both the vertical and horizontal axis:

$$\begin{aligned} w(s_1, s_2, s_3, s_4) &= \sum_{s'_1, s'_3} P_h(s_1, s'_1) P_h(s_3, s'_3) w(s'_3, s_2, s'_1, s_4), \\ w(s_1, s_2, s_3, s_4) &= \sum_{s'_2, s'_4} P_v(s_2, s'_2) P_v(s_4, s'_4) w(s_1, s'_4, s_3, s'_2) \end{aligned} \quad (7)$$

with

$$P_h = P_h^+, \quad P_h^2 = 1, \quad P_v = P_v^+, \quad P_v^2 = 1 \quad (8)$$

For spin models, the matrices  $P_h$  and  $P_v$  are equal to the identity. For  $k$ -mer models, it will not be the case anymore. The transfer matrices  $T_i$  and the corner transfer matrices  $C_i$  are also expected to be symmetric under these two mirror transformations. As a consequence, it is sufficient to consider  $C_1$  and the two transfer matrices  $T_1$  and  $T_2$ . Other matrices will be reconstructed from these three. The first step of the algorithm consists in extending the corner transfer matrix by adding the two transfer matrices,  $T_1$  and  $T_2$ , and a vertex  $w$ :

$$C'_1((s_4, s_5), (s_3, s_8)) = \sum_{s_1, s_2, s_6, s_7} w(s_1, s_2, s_3, s_4) \times T_1^{s_1}(s_5, s_6) C_1(s_6, s_7) T_2^{s_2}(s_7, s_8) \quad (9)$$

$(s_4, s_5)$  denotes a product state constructed from the states  $s_4$  and  $s_5$ . The process is represented diagrammatically on the figure (second diagram from the left on the top row). To reduce the dimension of  $C_1$ , a decomposition into singular values (SVD) is performed on  $C_1$ . The latter is replaced by a diagonal matrix whose elements are the largest

singular values  $\Lambda$ :

$$C_1''(s_9, s_{10}) = U^T(s_9, (s_4, s_5))C_1'((s_4, s_5), (s_3, s_8)) \times V((s_3, s_8), s_{10}) = \Lambda_{s_9} \delta_{s_9, s_{10}}. \quad (10)$$

The number of singular values that are kept, and therefore the dimension of  $C_1''$ , is a fixed parameter. The transfer matrices  $T_1$  and  $T_2$  are then extended by contraction with a single vertex:

$$\begin{aligned} T_1'^{s_3}((s_4, s_5), (s_2, s_6)) &= \sum_{s_1} w(s_1, s_2, s_3, s_4) T_1^{s_1}(s_5, s_6), \\ T_2'^{s_4}((s_1, s_5), (s_3, s_6)) &= \sum_{s_2} w(s_1, s_2, s_3, s_4) T_2^{s_2}(s_5, s_6), \end{aligned} \quad (11)$$

and then renormalized by performing the appropriate basis change:

$$T_1''^{s_3} = U^T T_1'^{s_3} U, \quad T_2''^{s_4} = V T_2'^{s_4} V^T \quad (12)$$

To construct the other transfer matrices, the mirror transformations need to be extended and renormalized too. Setting initially  $P_1 = P_v$  and  $P_2 = P_h$ , the matrices are extended as

$$\begin{aligned} P_1'((s_1, s_2), (s_3, s_4)) &= P_v(s_1, s_3) P_1(s_2, s_4), \\ P_2'((s_1, s_2), (s_3, s_4)) &= P_h(s_1, s_3) P_2(s_2, s_4) \end{aligned} \quad (13)$$

i.e.  $P_1' = P_h \otimes P_1$  and  $P_2' = P_h \otimes P_2$  and then renormalized as

$$P_1'' = U^T P_1' U, \quad P_2'' = V P_2' V^T \quad (14)$$

Finally, the other transfer matrices are given by

$$C_2' = P_2 C_1^T, \quad C_3' = P_1 C_2'^T, \quad C_4' = C_1^T P_1 = P_2 C_3'^T \quad (15)$$

The algorithm can be iterated either until the lattice size reaches the desired one or until thermodynamic averages become stable, i.e. lattice size independent, up to some accuracy. The number of iterations needed for convergence depends strongly on the proximity of a phase transition and on the number of states kept during the renormalization process. In the case of the  $k$ -mer model, we observed that convergence depends also on the boundary conditions. A faster convergence is usually obtained with random initial tensors. However, thermodynamic averages display oscillations as the lattice size is increased and for many points of the phase diagram, mostly in the nematic phase, we were not able to reach convergence at large number of states. Therefore, in the following, the study is limited to finite-size systems.

## 2.2 Statistical weight of a vertex

In the monomer-dimer model, each site of the lattice is occupied by a monomer. Dimers correspond to a bond joining two neighboring sites. A monomer can belong at

most to one dimer. A configuration of the system is therefore given by the set of bonds on which lies a dimer. A state, 0 or 1, is assigned to all bonds of the lattice. 0 indicates the absence of a dimer while 1 corresponds to the presence of a dimer. On a given site, the statistical weight of an isolated monomer is

$$w(0, 0, 0, 0) = 1, \quad (16)$$

while for a monomer that belongs to an horizontal dimer

$$w(1, 0, 0, 0) = w(0, 0, 1, 0) = e^{\mu_h} \quad (17)$$

and to a vertical dimer

$$w(0, 1, 0, 0) = w(0, 0, 0, 1) = e^{\mu_v} \quad (18)$$

All other elements of  $w$  are zero. Note that the factor  $\beta = 1/k_B T$  has been absorbed into the definition of the chemical potentials  $\mu_h$  and  $\mu_v$ .

A  $k$ -mer correspond to a sequence of  $k$  aligned monomers on the lattice. It can also be seen as a sequence of  $k - 1$  dimers on  $k - 1$  successive bonds of the lattice. The different dimers forming a  $k$ -mer needs to be distinguished. Therefore, a bond can be in  $k$  possible states. The state 0 denotes the absence of any dimer on the bond. Therefore, a vertex with four bonds in the state 0 signals the presence of an isolated monomer. The associated statistical weight is

$$w(0, 0, 0, 0) = 1, \quad (19)$$

The  $k$ -mers are decomposed into  $k - 1$  dimers labeled 1 to  $k - 1$  from left to right and bottom to top. For an horizontal  $k$ -mer, the statistical weights are

$$\begin{aligned} w(1, 0, 0, 0) &= w(2, 0, 1, 0) = \dots \\ &= w(k - 1, 0, k - 2, 0) = w(0, 0, k - 1, 0) = e^{\mu_h} \end{aligned} \quad (20)$$

while, for a vertical dimer, the non-vanishing elements are

$$\begin{aligned} w(0, 1, 0, 0) &= w(0, 2, 0, 1) = \dots \\ &= w(0, k - 1, 0, k - 2) = w(0, 0, 0, k - 1) = e^{\mu_v}. \end{aligned} \quad (21)$$

The image of a  $k$ -mer under a mirror transformation is still a  $k$ -mer but with dimers labeled in the reversed order. Therefore, the mirror tensors  $P_h$  and  $P_v$  satisfies

$$P_{h,v}(k - 1, 1) = P_{h,v}(k - 2, 2) = \dots = 1 \quad (22)$$

and all other elements vanish.

To be able to compare the entropy and the entanglement entropy of  $k$ -mer model with those of well-known lattice spin models, the algorithm was also applied to the  $q$ -state Potts and clock models. In both cases, a  $q$ -state spin degree of freedom is placed on each bond of the square lattice. The vertex considered above is therefore a plaquette of four spins. The statistical weight is

$$w(s_1, s_2, s_3, s_4) = e^{[V(s_1, s_2) + V(s_2, s_3) + V(s_3, s_4) + V(s_4, s_1)]/k_B T} \quad (23)$$

where  $V(s, s') = \delta_{s, s'}$  for the Potts model and  $V(s, s') = \cos \frac{2\pi}{q}(s - s')$  for the  $q$ -state clock model.

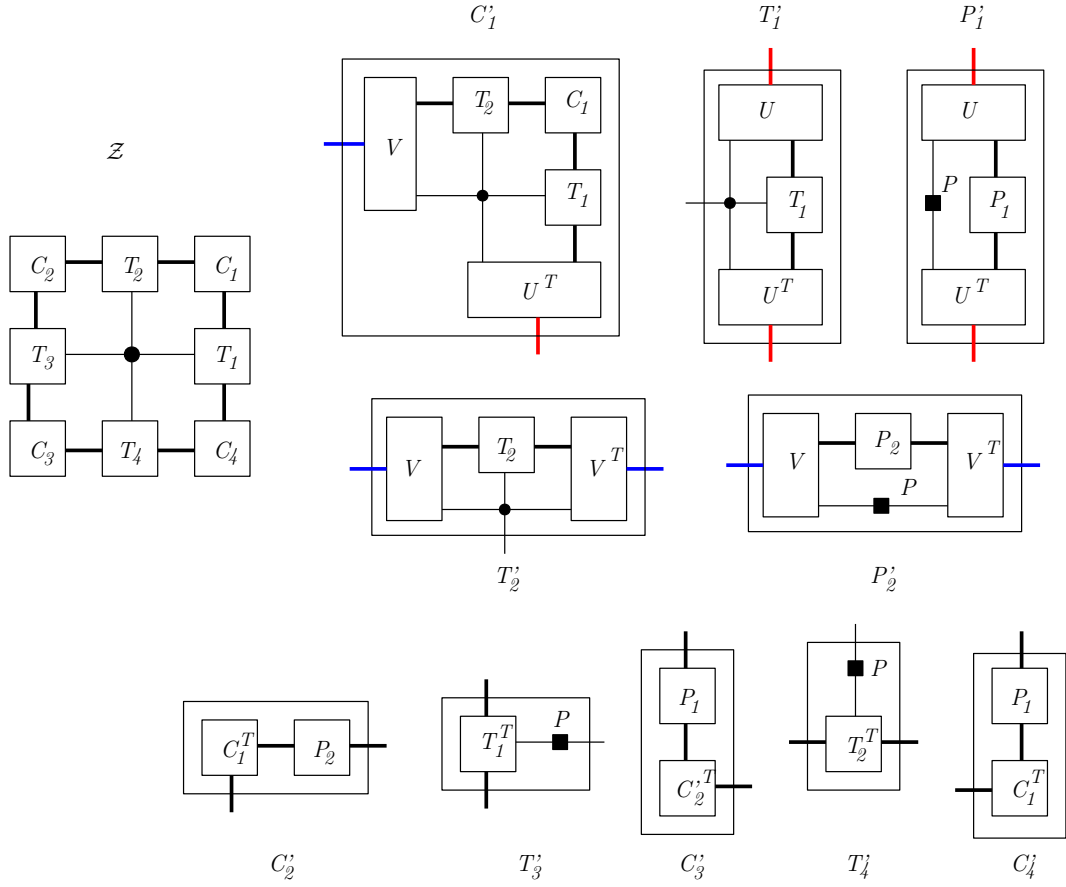


**Fig. 2.** Diagrammatic description of the CTMRG algorithm for the  $k$ -mer model. On the left, the partition function  $Z$  is decomposed into 8 tensors, 4 transfer matrices  $T_i$  and 4 corner transfer matrices  $C_i$ . The 4-leg black circle represents the statistical weight  $w$  on the central vertex. On each internal line, a sum over all possible states is implicitly performed. Thick lines are associated to renormalized states while thin lines were not renormalized yet. In the general case, the tensors  $T_i$  and  $C_i$  are independent. At the center of the first line, the corner transfer matrix  $C_1$  is first extended by contraction with the two transfer matrices  $T_1$  and  $T_2$  and a weight  $w$ . The resulting tensor is decomposed into singular values (SVD) corresponding to changes of basis  $U$  and  $V^T$  on its two external legs. Similarly, the transfer matrices  $T_1$  and  $T_2$  are extended by contraction with a weight  $w$  and the same change of basis  $U$  or  $V$  is applied. Without any truncation of  $U$  and  $V$ , the partition function is unchanged. On the right of the first and second lines, the horizontal and vertical mirror operators  $P$  are extended and the change of basis is applied. Using these mirror symmetries, the corner transfer matrices  $C_2$ ,  $C_3$  and  $C_4$  can be constructed from  $C_1$ . Transfer matrices  $T_3$  and  $T_4$  are obtained from  $T_1$  and  $T_2$ .

### 2.3 Boundary conditions

Different boundary conditions can be imposed to the system, provided that they are symmetric under horizontal and vertical mirror transformations. For Open Boundary Conditions (OBC), the initial  $T_1$  and  $C_1$  tensors are

$$\begin{aligned} T_1^{s_3}(s_4, s_2) &= \sum_{s_1} w(s_1, s_2, s_3, s_4), \\ C_1(s_4, s_3) &= \sum_{s_1, s_2} w(s_1, s_2, s_3, s_4) \end{aligned} \quad (24)$$

For Fixed Boundary Conditions (FBC) in the state  $s = 1$  for example, they are chosen to be

$$T_1^{s_3}(s_4, s_2) = w(1, s_2, s_3, s_4), \quad C_1(s_4, s_3) = w(1, 1, s_3, s_4). \quad (25)$$

In the  $k$ -mers model with  $k \geq 7$ , the system is expected to be in a nematic phase for intermediate chemical potentials. In the latter, the  $k$ -mers are mostly either horizontal or vertical ( $\mathbb{Z}_2$  symmetry). In the second case, horizontal bonds are in the state 0 while vertical ones are in states between 1 and  $k$ . To break the  $\mathbb{Z}_2$  symmetry of the nematic phase, mixed boundary conditions are imposed on the system. On the left and right boundaries, the horizontal bonds are forced to be in the state 0. On the upper and lower boundaries, vertical bonds can be in any of the states 1 to  $k - 1$  but not 0. This conditions are implemented in the initial tensors as

$$\begin{aligned} C_1(s_4, s_3) &= \sum_{s_2=1}^{k-1} w(0, s_2, s_3, s_4), \\ T_1^{s_3}(s_4, s_2) &= w(0, s_2, s_3, s_4), \end{aligned}$$

$$T_2^{s_4}(s_1, s_3) = \sum_{s_2=1}^{k-1} w(s_1, s_2, s_3, s_4) \quad (26)$$

Other initial tensors are obtained by applying the mirror transformations (15).

## 2.4 Observables

The free energy density  $f$  can be estimated from the partition function  $\mathcal{Z}$ . However, the convergence of this estimator is quite slow. A much faster convergence is obtained with the estimator

$$f = -\log \max T_1. \quad (27)$$

Finite differences of this free energy at two close chemical potentials  $\mu$  and  $\mu + \Delta\mu$  give access to the average density of  $k$ -mers

$$\langle n \rangle = -\frac{\partial f}{\partial \mu} \simeq -\frac{f(\mu + \Delta\mu) - f(\mu)}{\Delta\mu}. \quad (28)$$

This estimator is quite stable with  $\Delta\mu \simeq 10^{-2}$ . It is nevertheless more convenient to measure the average density on the central vertex. The statistical weight on the central vertex is indeed easily computed as

$$\rho(s_1, s_2, s_3, s_4) = \frac{1}{\mathcal{Z}} w(s_1, s_2, s_3, s_4) \times \text{Tr} [T_1^{s_1} C_1 T_2^{s_2} C_2 T_3^{s_3} C_3 T_4^{s_4} C_4] \quad (29)$$

which corresponds to connecting the four arms of the central vertex to four Transfer Matrices and inserting four Corner Transfer Matrices to recover the square lattice. The construction is similar to (6) for the partition function. At the  $n$ -th iteration of the algorithm, the total lattice size is therefore  $L = 2n + 3$ . Average densities of horizontal (vertical)  $k$ -mers  $\langle n_h \rangle$  ( $\langle n_v \rangle$ ) are computed on the two horizontal (vertical) bonds of the central vertex as

$$\langle n_{h,v} \rangle = \text{Tr} \rho n_{h,v} \quad (30)$$

where  $n_{h,v}(s_1, s_2, s_3, s_4) = 1$  when there is an horizontal (vertical) dimer in the bond configuration  $(s_1, s_2, s_3, s_4)$ . Due to the boundary conditions imposed to the system, these two densities take different values in the nematic phase. An order parameter is then defined as

$$Q = \frac{\langle n_h \rangle - \langle n_v \rangle}{\langle n_h \rangle + \langle n_v \rangle}. \quad (31)$$

The entropy of the central vertex embedded in the rest of the system can also be computed as

$$S = - \sum_{s_1, s_2, s_3, s_4} \rho(s_1, s_2, s_3, s_4) \log \rho(s_1, s_2, s_3, s_4) \quad (32)$$

using the statistical weight (29). It is a strictly local quantity that should not be confused with the entropy per site.

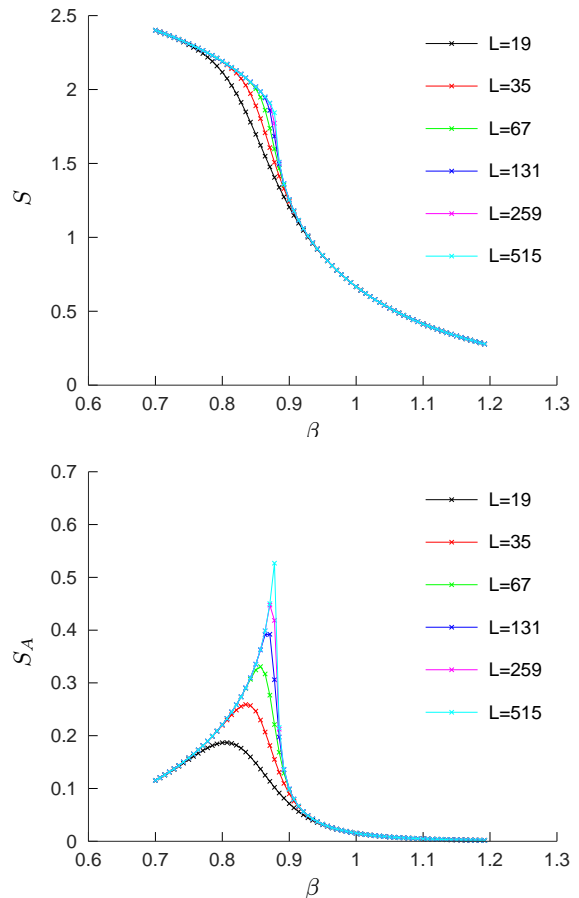


**Fig. 3.** Entropy at the central vertex (top) and von Neumann entanglement entropy (bottom) of the 2-state Potts model (equivalent to the Ising model) with Fixed Boundary Conditions versus the inverse of the temperature  $\beta = 1/k_B T$ . The different curves correspond to the different lattice sizes indicated in the legend. The data were computed with 32 states.

$S$  is nevertheless expected to be singular at phase transitions. To allow for comparison and identify the nature of the phase transitions of the 7-mer model, different spin models undergoing second-order, first-order and topological phase transitions were studied using the same CTMRG algorithm. As shown on figure 3, a break in the slope of  $S$  can be observed at the critical temperature of the Ising model. In the paramagnetic phase, the data shows that  $S$  behaves as  $|\beta - \beta_c| \ln |\beta - \beta_c|$  over a broad range of temperatures. This is also the case in the paramagnetic phase with Open Boundary Conditions. For the 7-state Potts model, which undergoes a first-order phase transition, the entropy  $S$  displays a jump at the transition temperature (figure 4). In the clock model, the entropy is observed to increase with the lattice size in the intermediate critical phase (figure 5).

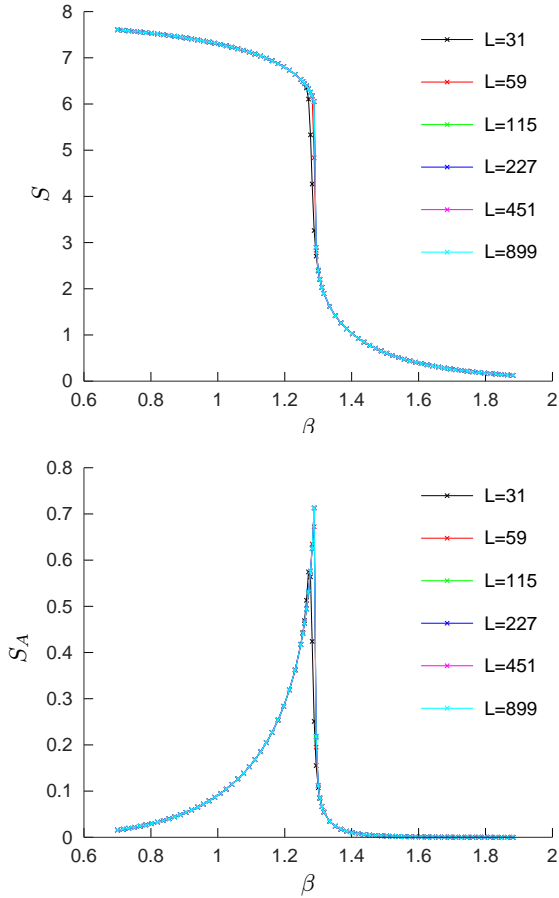


**Fig. 4.** Entropy of the central vertex (top) and von Neumann entanglement entropy (bottom) of the 7-state Potts model with Fixed Boundary Conditions versus the inverse of the temperature  $\beta = 1/k_B T$ . The different curves correspond to the different lattice sizes indicated in the legend. The data were computed with 147 states.

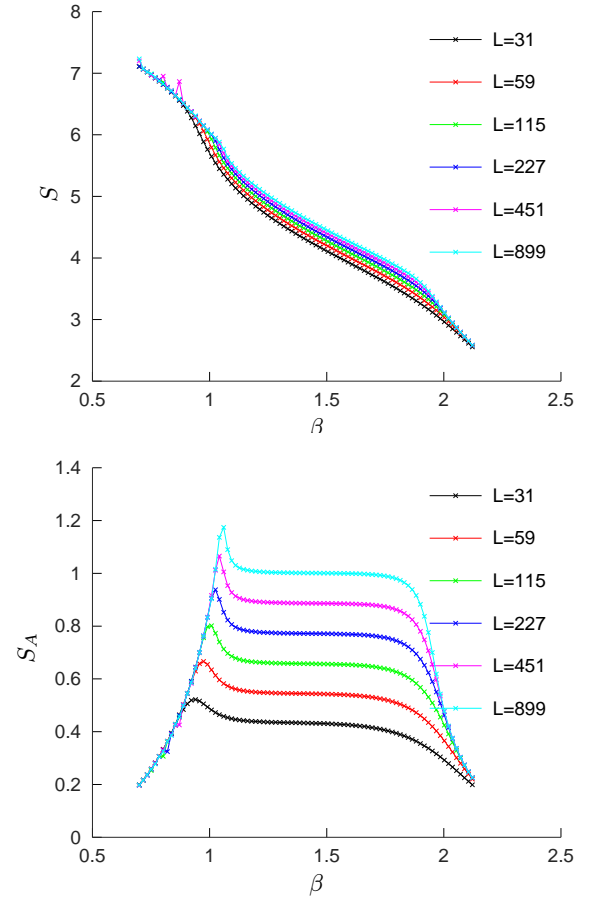


**Fig. 5.** Entropy of the central vertex (top) and von Neumann entanglement entropy (bottom) of the 7-state clock model with Fixed Boundary Conditions versus the inverse of the temperature  $\beta = 1/k_B T$ . The different curves correspond to the different lattice sizes indicated in the legend. The data were computed with 343 states.

## 2.5 Entanglement entropies

As mentioned in the introduction, an  $L \times L$  square lattice is considered and a cut of size  $L/2$  is made from the center of the square to the midpoint of one of its edges (see figure 38).  $L/2$  bonds are pending above the cut and  $L/2$  below. Consider a partially summed partition function  $\tilde{Z}_{s_1, s_2, \dots}^{s'_1, s'_2, \dots}$  of the system as a function of the not summed-up states  $s_1, s_2, \dots$  above the cut and  $s'_1, s'_2, \dots$  below the cut. The partition function  $\mathcal{Z}$  can be reconstructed in the following

$$\mathcal{Z} = \sum_{s_1, s_2, \dots, s'_1, s'_2, \dots} \tilde{Z}_{s_1, s_2, \dots}^{s'_1, s'_2, \dots} \delta_{s_1, s_2, \dots, s'_1, s'_2, \dots} \quad (33)$$

The quantity

$$\rho_A(s_1, s_2, \dots; s'_1, s'_2, \dots) = \frac{\tilde{Z}_{s_1, s_2, \dots}^{s'_1, s'_2, \dots}}{\mathcal{Z}} \quad (34)$$

can be interpreted as the elements of a reduced density matrix. The definition of the entanglement entropy be-

tween the degrees of freedom lying in the left and right halves of the system follows:

$$S_A = -\text{Tr} \rho_A \ln \rho_A. \quad (35)$$

By construction, the partition function of the square lattice with a cut is given by the fourth power of the Corner Transfer Matrix [30]:

$$\rho_A = \frac{C^4}{\text{Tr} C^4}. \quad (36)$$

For spin models (Ising, Potts, clock, ...), the entanglement entropy is easily computed from the eigenvalues of the Corner Transfer Matrix. Taking the partial sum of the four Corner Transfer Matrices, cf. Eqs. (34) and (36), results in the reduced density matrix  $\rho_A$  well-known in CTMRG [43]. In the case of the  $k$ -mer model, the corner transfer matrices  $C_i$  are not symmetric. Nevertheless, the relations (15) show that the reduced density matrix can

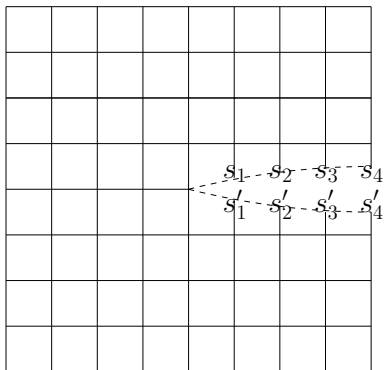


**Fig. 6.** Cut made on the right side of a square lattice defines the reduced density matrix  $\rho_A$  in order to measure the entanglement entropy between the degrees of freedom lying on the left and the right rectangular-shaped halves of the square lattice..

be written as

$$\rho_A = C_4 C_3 C_2 C_1 = (C_1^T C_1)^2. \quad (37)$$

The matrix  $C_1^T C_1$  is symmetric and its eigenvalues are the square of the singular values of  $C_1$  computed at each iteration. Therefore, the von Neumann entanglement entropy is easily computed as

$$S_A = - \sum_i A_i^4 \ln A_i^4 \quad (38)$$

where the  $A_i$ 's are proportional to the singular values of  $C_1$  with the constraint  $\sum_i A_i^4 = 1$ . The Renyi entropy is defined as

$$S_n = \frac{1}{1-n} \ln \left[ \sum_i A_i^{4n} \right]. \quad (39)$$

In contrast to the entropy of the central vertex previously defined, the entanglement entropy is a non-local quantity that depends on long-range correlations in the system.

Numerical data for the 2-state Potts model (equivalent to the Ising model) are presented on the right of figure 3. As the lattice size is increased, the peak of the entanglement entropy becomes sharper and occurs at a temperature closer to the critical point  $\beta_c = \ln(1 + \sqrt{2}) \simeq 0.881$ . Numerical data for the entanglement entropy of the 7-state Potts model, which undergoes a first-order phase transition at  $\beta_t = \ln(1 + \sqrt{7}) \simeq 1.294$ , are presented on the right of figure 4. A sharp peak and a discontinuity are observed at the transition temperature. Finally, the entanglement entropy of the 7-state clock model is presented on figure 5. As shown in [13], the entanglement entropy grows with the lattice size in the whole intermediate critical phase. The two Kosterlitz-Thouless phase transitions are revealed by two peaks observed respectively with FBC and OBC.

As mentioned in the introduction, at the critical point the entanglement entropies are expected to scale with the

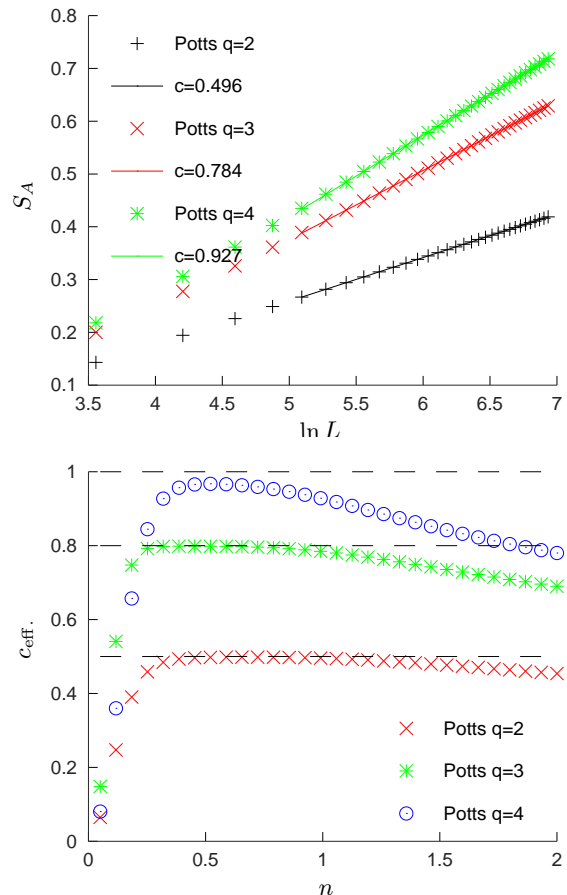


**Fig. 7.** On the top figure, Finite-Size Scaling of the von Neumann entanglement entropies  $S_A$  of the  $q = 2, 3$  and 4-state Potts models at their critical point  $\beta_c = \log(1 + \sqrt{q})$ . The continuous lines are linear fits of the data. The central charges, estimated from the slopes, are given in the legend. On the bottom figure, the effective charges extracted from a linear fit of the Renyi entropies  $S_n$  are plotted versus  $n$ . The expected values are displayed as dashed lines.

length  $\ell$  of the cut as

$$S_A \sim \frac{c}{6} \ln \ell, \quad S_n \sim \frac{c}{12} \left( 1 + \frac{1}{n} \right) \ln \ell. \quad (40)$$

On figure 7, the entanglement entropies  $S_A$  and  $S_2$  are plotted versus the logarithm of the size  $L$  of the cut for the  $q = 2, 3$  and 4-state Potts models at their critical point. As expected, the entropies display a linear behavior with  $\log L$ . Assuming that, for the von Neumann entanglement entropy  $S_A$ , the prefactor is the same as in the strip geometry (40), the estimates of the central charge are compatible with the known values  $c = 1, 4/5$  for the 2 and 3-state Potts models respectively. The data for the 4-state Potts model, whose central charge is known to be  $c = 1$ , are slightly away from the theoretical prediction, maybe due to the fact that the critical point is actually a tricritical point involving stronger corrections. For the Renyi entropy  $S_n$ , the expected prefactor is recovered for



values of  $n$  around  $n \simeq 1/2$ . For larger values of  $n$ , strong deviations are observed.

## 2.6 Convergence and error bars

Provided that there is no source of systematic deviations (due to insufficient thermalization or lack of ergodicity), error bars in Monte Carlo simulations result only from statistical fluctuations. The latter can be made as small as desired by increasing the number of Monte Carlo steps. In CTRMG, the only source of error is the truncation of the Corner Transfer Matrix. The dimension of the latter increases exponentially fast with the lattice size. If all states were kept, the calculation would be exact. By increasing the number of states kept at each truncation, the deviation from the exact result can be made smaller. However, in contrast to Monte Carlo simulations, it is not possible to estimate the systematic deviation introduced by the truncation of the Corner Transfer Matrix. Therefore, in the rest of the paper, the observables are usually plotted for different number of states to show the convergence of the data.

In DMRG studies, the level of approximation is often quantified with the so-called truncation error. The latter is defined as the sum of the eigenvalues of the density matrix that are discarded. The equivalent of the density matrix in CTMRG is  $C^4$ , the fourth power of the Corner Transfer Matrix. In our implementation, a Singular Value Decomposition of  $C$  is performed at each iteration and a small number  $m$  of singular values  $\Lambda$  are kept while the rest is discarded and the matrices are truncated. A possible definition of a truncation error for CTMRG is therefore

$$\varepsilon = \frac{\sum_{i=m}^N \Lambda_i^4}{\sum_{i=1}^N \Lambda_i^4}$$

The smallest the truncation error and the more accurate the simulation. However, it is not possible to establish a simple relation between the truncation error and the error bar on the observables computed in CTMRG (free energy, order parameter entanglement entropy, ...). It is a major drawback of the method, shared with DMRG and all Matrix-Product and Tensor-Network algorithms. In the simulations whose results are presented in the paper, only the  $m$  largest singular values of the Corner Transfer Matrix are computed at each iteration using the `Arpack` library. To discuss the behavior of the truncation error with the simulation parameters, we have implemented a (slower) version of the code where all singular values are computed (with `Lapack`). It allows for the computation of the truncation error at each iteration but for smaller systems.

As can be seen on figure 8 for the 7-mer model, the truncation error increases very rapidly with the chemical potential. The accuracy is therefore expected to be much better in the low-density phase than in the high-density phase. The truncation error displays a decay with the number of states  $m$  which is close to a power-law. For  $\mu = 1.2$ , the exponent of this power-law decay is  $-1.8$ .

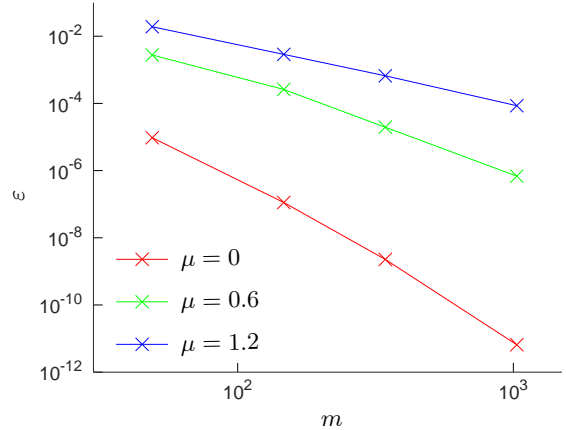


**Fig. 8.** Truncation error of the 7-mer model versus the number of states  $m$  for  $\mu = 0, 0.6$  and  $1.2$  and a lattice size  $L = 51$ .

## 3 Numerical evidences of phase transitions in the $k$ -mer model

The 7-mer model is studied by means of the CTMRG algorithm keeping a number of states equal to 343, 686 or 1029. During each simulation, the calculation is stopped after 14, 28, 56, 112, 224 and 448 iterations, which corresponds respectively to lattice sizes 31, 59, 115, 227, 451 and 899. The different observables are then computed. To allow for comparison, the 6-mer and 8-mer model were also studied. In the latter, 512 states were kept and the observables were computed for the lattice sizes 35, 67, 131, 259, 515 and 1027. For the former, 648 states were kept and the observables were computed for the lattice sizes 27, 51, 99, 195, 387 and 771.

### 3.1 Average density

As shown on figure 9, the average total density  $\langle n \rangle = \langle n_v \rangle + \langle n_h \rangle$  (30) of 7-mers increases monotonously with the chemical potential  $\mu$ . For negative chemical potentials, the average density depends only very weakly on the lattice size. In the intermediate range  $0.2 - 1.0$ , stronger finite-size effects are observed for the smallest lattice size,  $L = 31$ . For large chemical potentials, finite-size corrections are again weaker but a different sign than in the intermediate region. The assumption of the existence of three different phases, as made in the literature on the basis of Monte Carlo simulations, would fit with these observations. Note that the same observations can be made from the data of the 8-mer model. For the 6-mer model, for which no transition is expected, finite-size effects are nevertheless observed at intermediate chemical potentials.

### 3.2 Order parameter of the nematic phase

On figure 10, the order parameter  $Q$  (31) of the 7-mer model is plotted versus the chemical potential. Figure 10

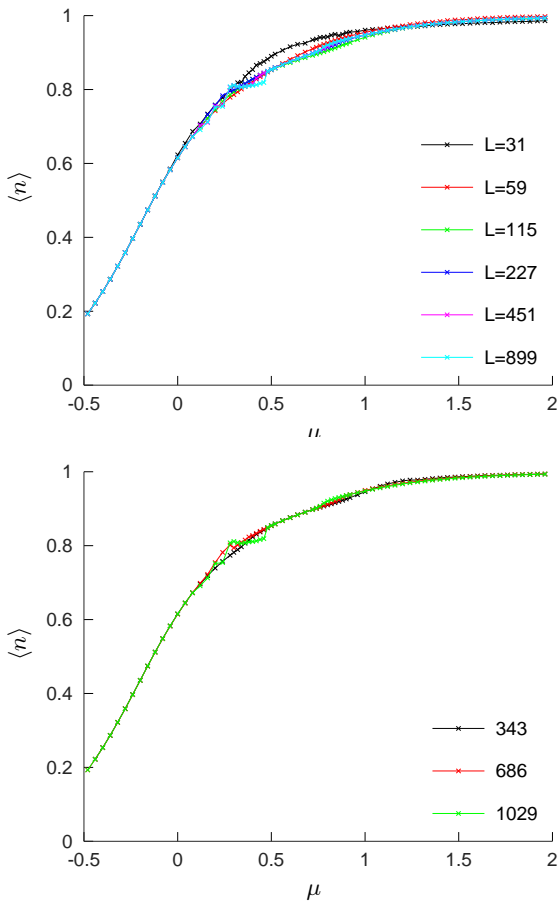


**Fig. 9.** Average density of the 7-mer model versus the chemical potential  $\mu$  per monomer. On the top figure, the data were computed using CTMRG with 1029 states and the different curves correspond to different lattice sizes  $L$  as indicated by the legend. On the bottom figure, the lattice size is fixed to  $L = 899$  but different numbers of states were kept in the CTMRG algorithm (343 in black, 686 in red and 1029 in green).

(right) shows that the location of the phase boundaries depends non only on the lattice size but also on the number of states kept during the CTMRG calculation. Despite the important computational effort devoted to this study, an extrapolation of the chemical potentials at the transition remains elusive. For sufficiently large lattice sizes, the same shape as observed in Monte Carlo simulations [31] is obtained with CTMRG. For a lattice size  $L = 899$  and keeping 1029 states during the renormalization of the corner transfer matrix, the boundaries of the nematic phase, signaled by a non-vanishing order parameter  $Q$ , can be estimated at the chemical potentials per monomer  $\mu_1 \simeq 0.46$  and  $\mu_2 \simeq 0.91$ . The second value is quite far from the Monte Carlo estimate  $\mu_2 \simeq 0.795$  [37]. However, figure 10 shows that the nematic phase tends to shrink as the lattice size is increased so an extrapolation may eventually give a closer estimate of  $\mu_2$  in the thermodynamic limit. The average densities at the transitions are estimated to be  $\langle n_1 \rangle \simeq 0.83$  and  $\langle n_2 \rangle \simeq 0.91$  to be compared with the

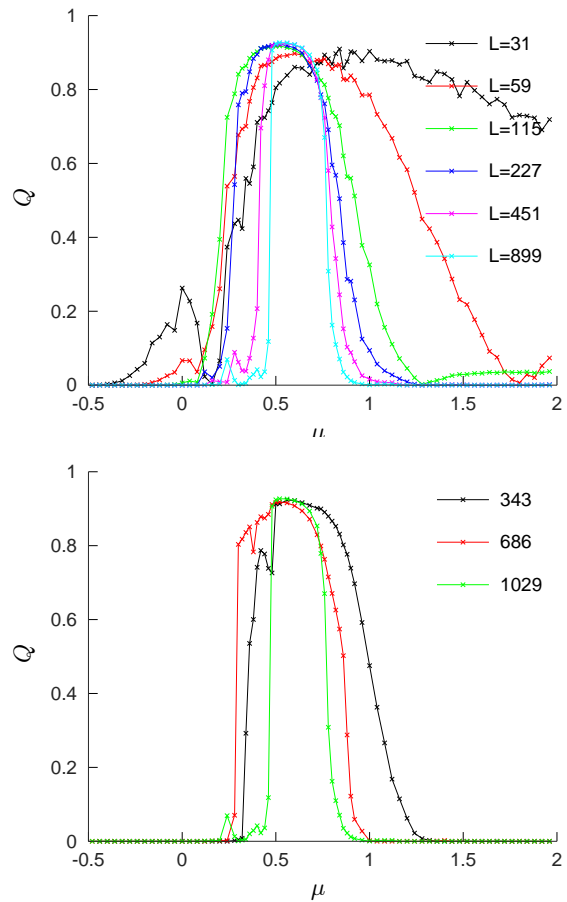


**Fig. 10.** Order parameter of the nematic phase of the 7-mer model versus the chemical potential  $\mu$  per monomer. On the top figure, the data were computed using CTMRG with 1029 states and the different curves correspond to different lattice sizes  $L$  as indicated by the legend. On the bottom figure, the lattice size is fixed to  $L = 899$  but different numbers of states were kept in the CTMRG algorithm (343 in black, 686 in red and 1029 in green).

Monte Carlo estimates  $\langle n_1 \rangle \simeq 0.745$  and  $\langle n_2 \rangle \simeq 0.915(15)$ . In contrast to the chemical potentials, the CTMRG and Monte Carlo estimates of the density at the second transition are nicely compatible due to the fact that the average density varies slowly with the chemical potential.

For comparison, the order parameter  $Q$  of the 6-mer and 8-mer models are presented on figure 11. In the case of the 6-mer model, the order parameter vanishes as the lattice size is increased indicating the absence of any intermediate nematic phase. In contrast, in the case of the 8-mer model, the order parameter saturates over a wide range of chemical potentials.

### 3.3 Entropy of the central vertex

In the  $k$ -mer model, a single monomer lies on each site of the square lattice. Therefore, the entropy of the central

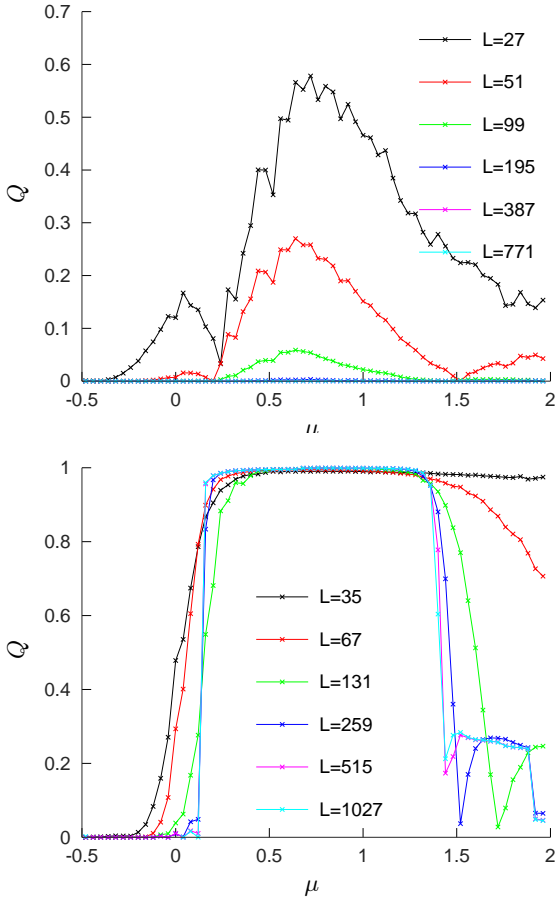


**Fig. 11.** Order parameter of the nematic phase of the 6-mer model (top) and of the 8-mer model (bottom) versus the chemical potential  $\mu$  per monomer. The data were computed using CTMRG with 648 states for the 6-mer model and 512 for the 8-mer model. The different curves correspond to different lattice sizes  $L$  as indicated by the legend.

vertex is a local quantity, as the average density. Considering the fact that a site may be empty with a probability  $1 - \langle n \rangle$  or occupied by any of the  $k$  possible monomers forming either a horizontal or a vertical  $k$ -mer with a probability  $\langle n \rangle / 2k$ , the entropy of the central vertex is

$$S_{\text{OBC}} = -(1 - \langle n \rangle) \ln(1 - \langle n \rangle) - 2k \times \frac{\langle n \rangle}{2k} \ln \frac{\langle n \rangle}{2k}. \quad (41)$$

In the nematic phase, the  $\mathbb{Z}_2$  orientational symmetry between horizontal and vertical  $k$ -mers is broken by FBCs and only one orientation of the  $k$ -mer is allowed. The entropy of the central vertex is then expected to be

$$S = -(1 - \langle n \rangle) \ln(1 - \langle n \rangle) - k \times \frac{\langle n \rangle}{k} \ln \frac{\langle n \rangle}{k}. \quad (42)$$

The entropy per monomer  $S/\langle n \rangle$  of the 7-mer model is plotted on figure 12. In the case of OBCs (presented in the inset), the curves are nicely compatible with (41) for sufficiently large number of states. Finite-Size corrections

remain small. With FBCs, a depletion appears in an intermediate range of chemical potentials. The entropy of the central vertex is close to (42) in this depletion while it remains nicely compatible with (41) outside. The existence of an intermediate nematic phase, sensitive to the boundary conditions unlike the two disordered phases, explains the numerical data. Like the order parameter, the depletion becomes thinner as the lattice size or the number of states is increased. For 1029 states, the curves of the two largest lattice sizes collapse between  $\mu_1 \simeq 0.47$  and  $\mu_2 \simeq 0.75$ . The first chemical potential is compatible with the location of the isotropic-nematic transition as estimated above from the order parameter  $Q$ . The second is smaller than the previous estimate but closer to the Monte Carlo estimate  $\mu_2 \simeq 0.795$  [37].

For comparison, the entropies of the central vertex for the 6-mer and 8-mer models are presented on figures 13. In the case of the 6-mer model, the entropy per monomer  $S/\langle n \rangle$  is compatible with (41) for all considered chemical potentials. There is no signature of a nematic phase in this case. For the 8-mer model, the entropy  $S$  displays a wide flat depletion where it is compatible with (42). For large chemical potential, the entropy of the central vertex has not returned to the value predicted by (41), as expected in the disordered phase. It is not clear whether the transition nematic-isotropic is absent or the number of states is still too small to achieve convergence.

#### 4 Entanglement entropies of the $k$ -mer model

The von Neumann entanglement entropy is presented on figure 14 for the 7-mer model. Apart from the two points out of the curve in the disordered phase, the entanglement entropy grows monotonously with the chemical potential  $\mu$ . In particular, no peak is observed, even at large lattice sizes, in apparent contradistinction with the assumption that the two transitions are continuous. A small dependence with the lattice size is observed. However, this dependence is similar to the one displayed by the average density (figure 9) and differs from the one of the 7-state clock model in its critical phase (figure 5). Therefore, the usual signature of a first, second order and even Berezinskii-Thouless transition is absent in the 7-mer model. Increasing the number of states of the CTMRG algorithm does not change the situation. In contrast, the entanglement entropy of a quantum state approximated by a MPS is known to be bounded by a function of the logarithm of the dimension of the auxiliary space [45,46,47]. A relation similar to this one should hold for the truncated corner transfer matrices. However, it can be observed on figure 14 that the variation of the entanglement entropy is very small (and mostly negative!) when extending the number of states from 686 to 1029. Therefore, the upper bound on the entanglement entropy imposed by the number of states used in the calculations is not reached and it can be considered that the estimated entanglement entropy has already reached its exact value with the considered numbers of states. With OBC, the curve is very similar. Only finite-size corrections seems to depend on

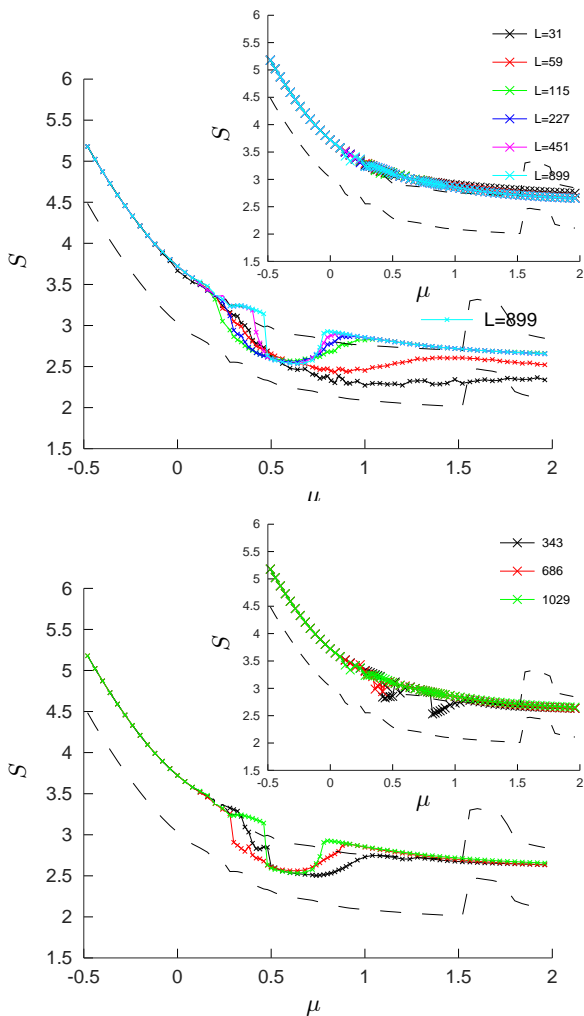


**Fig. 12.** Entropy of the central vertex of the 7-mer model versus the chemical potential  $\mu$  per monomer. On the top figure, the data were computed using CTMRG with 1029 states and the different curves correspond to different lattice sizes  $L$  as indicated by the legend. On the bottom figure, the lattice size is fixed to  $L = 899$  but different numbers of states were kept in the CTMRG algorithm (343 in black, 686 in red and 1029 in green). In the inset, the same quantities are plotted but with OBCs instead of FBCs. The two ansätze (41) and (42) are plotted as dashed lines.

boundary conditions. The curves are quite similar for the 6 and 8-mer models (figure 15). The entanglement entropy increases monotonously with the chemical potential. Only the sign of the Finite-Size correction differs.

The entanglement spectrum  $\rho_i = A_i^4 / \sum_i A_i^4$  is plotted on figure 16 at different chemical potentials. No significant difference between the 6, 7 and 8-mer model can be observed. The decay of  $\rho_i$  with  $i$  is slower than an exponential but faster than a simple power law. Moreover, the decay becomes slower as the chemical potential is increased. In contrast, in lattice spin models, the entanglement spectrum displays its slowest decay at the critical point and

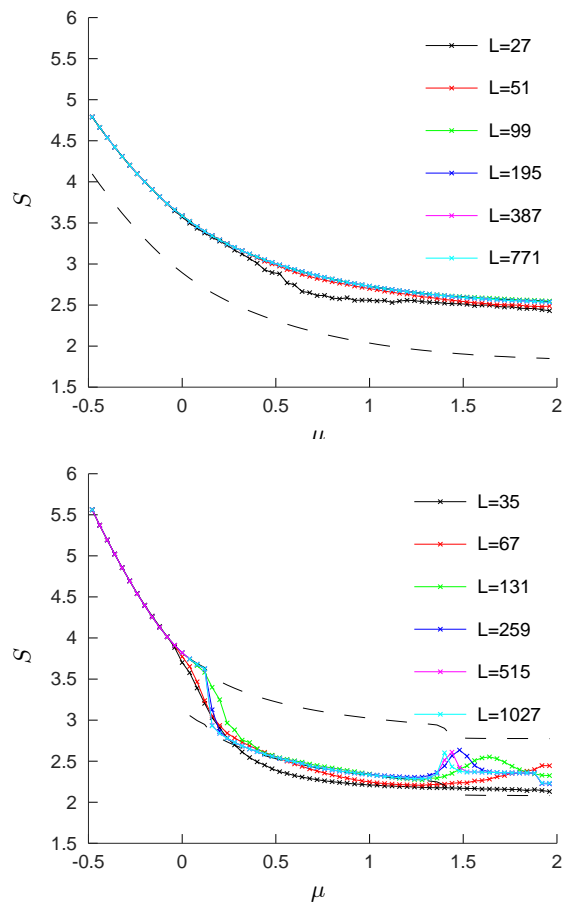


**Fig. 13.** Entropy of the central vertex of the 6-mer model (top) and of the 8-mer model (bottom) versus the chemical potential  $\mu$  per monomer. The data were computed using CTMRG with 648 states for the 6-mer model and 512 for the 8-mer model. The different curves correspond to different lattice sizes  $L$  as indicated by the legend. The two ansätze (41) and (42) are plotted as dashed lines using the numerical estimate of the density.

the decay becomes faster as the temperature moves away from the critical point.

## 5 Conclusions

The existence of two phase transitions for the  $k$ -mer model with  $k \geq 7$ , as previously shown by means of Monte Carlo simulations, is confirmed by the study of the order parameter and the entropy at the central vertex of a square lattice. However, the accuracy reached by our CTMRG computations is not sufficient to determine the critical behavior which is associated to these transitions in order to test the conjectures made from Monte Carlo simulations. Nevertheless, in our CTMRG calculations the entanglement entropy increases monotonously with the chemical potential. No peak is observed at the two transitions. In contrast, in the geometry considered in this work, the von Neumann and Renyi entanglement entropies of the  $q$ -state

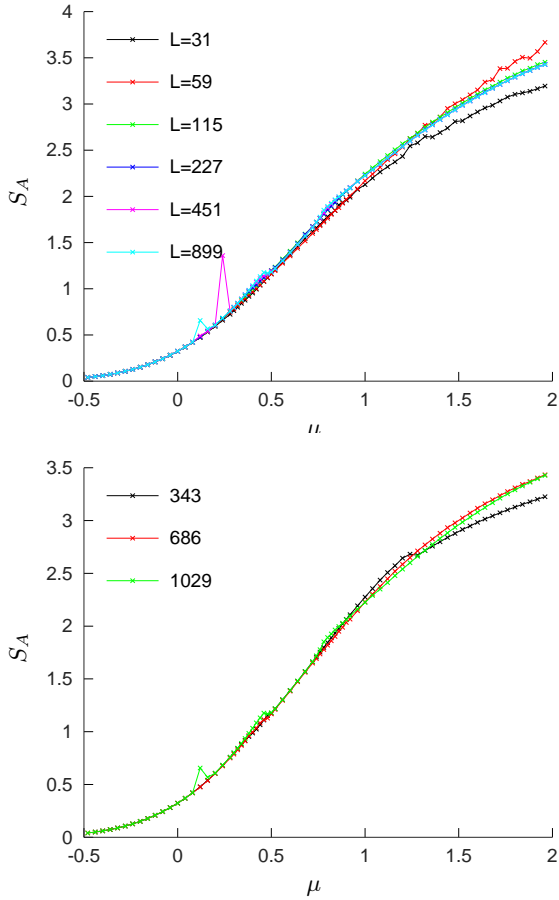


**Fig. 14.** Von Neumann entanglement entropy of the 7-mer model versus the chemical potential  $\mu$  per monomer. On the top figure, the data were computed using CTMRG with 1029 states and the different curves correspond to different lattice sizes  $L$  as indicated by the legend. On the bottom figure, the lattice size is fixed to  $L = 899$  but different numbers of states were kept in the CTMRG algorithm (343 in black, 686 in red and 1029 in green).

Potts model diverge as the logarithm of the lattice size at the critical temperature when  $q \leq 4$  and is discontinuous at the first-order transition when  $q > 4$ . We made CTMRG calculations of the Ising model with a number of states kept at each truncation of the corner transfer matrix as small as 2 and of the 7-state Potts model with only 7 states. The peak is shifted and rounded but is still present and clearly visible. We infer that the absence of peak of the entanglement entropy in the  $k$ -mer model cannot be explained by an insufficient number of states in our CTMRG calculations. Moreover, Conformal Field Theory predicts that the entanglement entropy diverges in a universal manner with the lattice size  $L$ , as  $\frac{c}{6} \ln L$  for the von Neumann entanglement entropy and  $\frac{c}{12} (1 + \frac{1}{n}) \ln L$  for the Renyi entropies (Fixed Boundary Conditions). It is therefore inferred that the two transitions of the  $k$ -mer model with  $k \geq 7$  cannot be in the universality class of the Ising model, despite the fact that a  $\mathbb{Z}_2$  symmetry is bro-

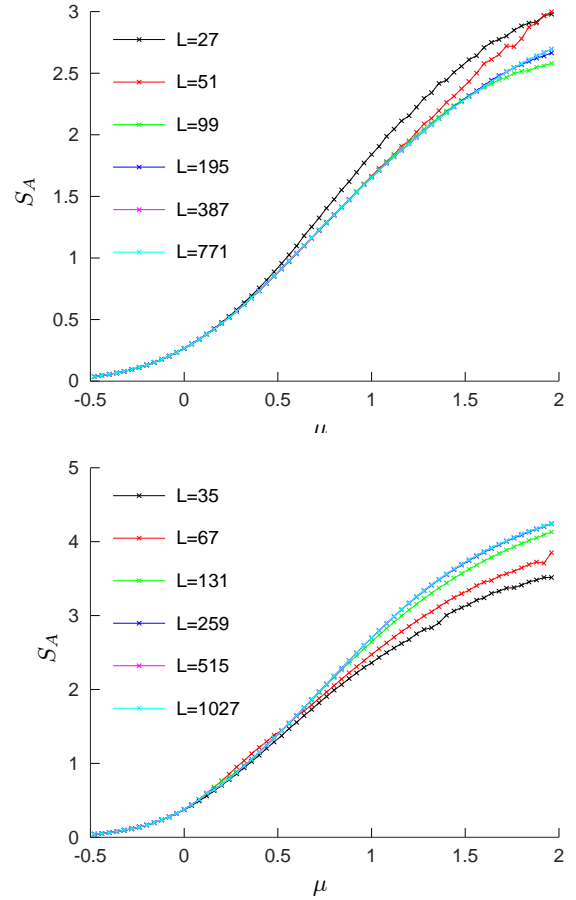


**Fig. 15.** Entanglement entropy of the 6-mer model (top) and of the 8-mer model (bottom) versus the chemical potential  $\mu$  per monomer. The data were computed using CTMRG with 648 states for the 6-mer model and 512 for the 8-mer model. The different curves correspond to different lattice sizes  $L$  as indicated by the legend.

ken in the nematic phase. Moreover, if the transitions are continuous, their long-distance behavior probably cannot be described by a Conformal Field Theory.

## Acknowledgements

The numerical simulations were performed at the Explor meso-center of the University of Lorraine. This research was partially supported by APVV-16-0186 (EXSES).

The two authors made an equal contribution to the paper.

## References

1. S.J. Gu, S.S. Deng, Y.Q. Li, and H.Q. Lin (2004) *Phys. Rev. Lett.* **93** 086402
2. Y. Chen, P. Zanardi, Z.D. Wang, and F.C. Zhang (2006) *New. J. Phys.* **8** 97



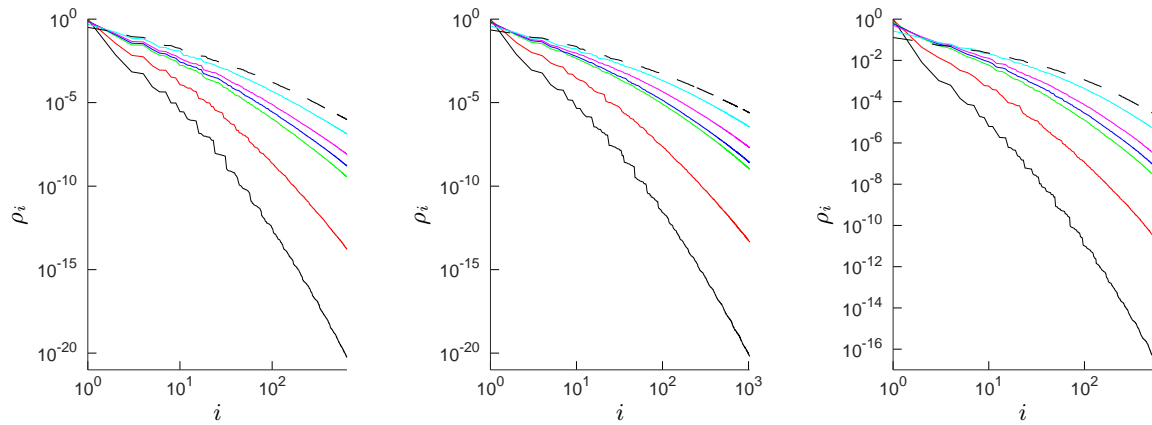


**Fig. 16.** Entanglement spectrum of the 6 (left), 7 (center), and 8-mer (right) models at the largest lattice size and with the largest number of states considered. The different curves correspond to chemical potentials  $-0.4, 0, 0.48, 0.6, 0.76, 1.24, 1.92$  (from bottom to top).

3. L. Amico, R. Fazio, A. Osterloh, and V. Vedral (2008) *Rev. Mod. Phys.* **80** 517
4. P. Calabrese, and J. Cardy. (2009) *J. Phys. A: Math. and Theor.* **42** 504005
5. P. Lajkó, and F. Iglói (2017) *Phys. Rev. E* **95** 012105
6. E. Fradkin, and L. Susskind (1978) *Phys. Rev. D* **17** 2637
7. H.F. Trotter (1958) *J. Math.* **8** 887
8. M. Suzuki (1966) *J. Phys. Soc. Jpn.* **21** 2274
9. M. Suzuki (1976) *Prog. Theor. Phys.* **56** 1454
10. H. Ueda, K. Okunishi, R. Krmar, A. Gendiar, S. Yunoki, T. Nishino (2017) *Phys. Rev. E* **96** 062112
11. C. Chatelain (2016) *J. Stat. Mech.* 073306
12. H. Ueda, K. Okunishi, K. Harada, R. Krmar, A. Gendiar, S. Yunoki, T. Nishino, [arXiv:2001.10176](https://arxiv.org/abs/2001.10176)
13. R. Krmar, A. Gendiar, T. Nishino (2020) [arXiv:2003.10718](https://arxiv.org/abs/2003.10718) accepted in *Acta Phys. Pol. A*
14. R.H. Fowler, and G.S. Rushbrooke (1937) *Trans. Faraday Soc.* **33** 1272
15. R. Kenyon (2003), [arXiv:math/0310326](https://arxiv.org/abs/math/0310326)
16. R. Kenyon (2009) [arXiv:0910.3129](https://arxiv.org/abs/0910.3129)
17. M.E. Fisher (1961) *Phys. Rev.* **124** 1664
18. P.W. Kasteleyn (1961) *Physica* **27** 1209
19. O.J. Heilmann, and E.H. Lieb (1970) *Phys. Rev. Lett.* **24** 1412
20. O.J. Heilmann, and E.H. Lieb (1972) *Commun. Math. Phys.* **25** 190
21. A. Ghosh, D. Dhar et J.L. Jacobsen (2007) *Phys. Rev. E* **75** 011115
22. F. Alet, J.L. Jacobsen, G. Misguich, V. Pasquier, F. Mila, and M. Troyer (2005) *Phys. Rev. Lett.* **94** 235702
23. F. Alet, Y. Ikhlef, J.L. Jacobsen, G. Misguich, and V. Pasquier (2006) *Phys. Rev. E* **74** 041124
24. L. Onsager (1949) *Annals of the New York Academy of Sciences* **51** 627
25. D. Frenkel (1999) *Physica A* **263** 26
26. R. Zwanzig (1963) *J. Chem. Phys.* **39** 1714
27. N.D. Mermin, and H. Wagner (1966) *Phys. Rev. Lett.* **17** 1133
28. J.P. Straley (1971) *Phys. Rev. A* **4** 675
29. D. Frenkel, and R. Eppenga (1985) *Phys. Rev. A* **31** 1776
30. I. Peschel, M. Kaulke, O. Legeza (1999) *Ann. Physik (Leipzig)* **8** 153
31. A. Ghosh, and D. Dhar (2007) *Eur. Phys. Lett.* **78** 20003
32. D.A. Matoz-Fernandez, D.H. Linares, and A.J. Ramirez-Pastor (2008) *Eur. Phys. Lett.* **82** 50007
33. D.A. Matoz-Fernandez, D.H. Linares, and A.J. Ramirez-Pastor (2008) *Phys. A* **387** 6513
34. D.A. Matoz-Fernandez, D.H. Linares, and A.J. Ramirez-Pastor (2008) *J. Chem. Phys.* **128** 214902
35. D.H. Linares, F. Roma, and A.J. Ramirez-Pastor (2008) *J. Stat. Mech.* **P03013**
36. T. Fischer and R.L.C. Vink (2009) *EPL* **85** 56003
37. J. Kundu, R. Rajesh, D. Dhar, J.F. Stilck (2013) *Phys. Rev. E* **87** 032103
38. R.J. Baxter (1968) *J. Math. Phys.* **9** 650
39. S.R. White (1992) *Phys. Rev. Lett.* **69** 2863
40. S.R. White (1993) *Phys. Rev. B* **14** 10345
41. U. Schollwoeck (2005) *Rev. Mod. Phys.* **77** 259
42. U. Schollwoeck. (2011) *Ann. Phys.* **1** 96
43. T. Nishino, and K. Okunishi (1996) *J. Phys. Soc. Japan* **4** 891
44. Baxter R.J. (1982) *Exactly Solved Models in Statistical Mechanics* (New York: Academic Press)
45. F. Verstraete, and J.I. Cirac (2005) [cond-mat:0505140](https://arxiv.org/abs/cond-mat/0505140)
46. N. Schuch, M.M. Wolf, F. Verstraete, and J.I. Cirac (2007) [arXiv:0705.0292](https://arxiv.org/abs/0705.0292)
47. F. Pollmann, S. Mukerjee, A. Turner, and J.E. Moore (2009) *Phys. Rev. Lett.* **102** 255701